# Thermodynamic Modeling of a Rotating Detonation Engine Through a Reduced-Order Approach

Tom Kaemming,* Matthew L. Fotia,† and John Hoke*
*Innovative Scientific Solutions, Inc., Dayton, Ohio 45459*
and
Fred Schauer‡
*U.S. Air Force Research Laboratory, Wright–Patterson Air Force Base, Ohio 45433*

DOI: 10.2514/1.B36237

**Reduced-order modeling of the thermodynamic cycle within a rotating detonation engine system is presented with an emphasis on the identification of the parameters that drive performance and the validation of the model with computational and experimental test results. Treatment of propellant injection and the balancing of pressure and mass flow through the engine are presented. A focus is placed on the identification of the parameters that drive performance in a rotating detonation device, such as deflagration of reactants, while noting those that have little impact, which include reduced detonation velocity due to lateral area relief. A thermodynamic description of the rotating detonation engine is proposed, using traditional cycle analysis methods in an effort to develop an initial design and performance tool for such pressure gain combustion devices.**



## Nomenclature

| | | |
|---|---|---|
| $A$ | = | area |
| $b$ | = | detonation wave pressure drop parameter |
| $C_p$ | = | specific heat at constant pressure |
| $F_g$ | = | gross thrust |
| $F_{sp}$ | = | specific thrust |
| $I_{sp}$ | = | specific impulse |
| $k$ | = | detonation wave pressure decay rate |
| $M$ | = | Mach number |
| $P$ | = | pressure |
| $s$ | = | specific entropy |
| $T$ | = | temperature |
| $t$ | = | time coordinate |
| $V$ | = | velocity |
| $\dot{w}$ | = | mass flow rate |
| $X$ | = | axial coordinate |
| $x$ | = | spatial coordinate |
| $Y$ | = | mass fraction |
| $\gamma$ | = | ratio of specific heats |
| $\delta$ | = | exit flow distortion |
| $\theta$ | = | oblique shock turning angle |
| $\tau$ | = | detonation channel width |
| $\tau_{drop}$ | = | pressure decay time parameter |
| $\tau_{factor}$ | = | pressure decay time correction factor |
| $\phi$ | = | equivalence ratio |

*Subscripts*

| | | |
|---|---|---|
| Air | = | air manifold quantity |
| Avg | = | average value |
| Def | = | deflagration property |
| Det | = | detonation wave property |
| Exit | = | rotating detonation engine exit quantity |
| Flame | = | deflagration flame quantity |
| Fuel | = | fuel manifold quantity |
| Inj | = | propellant injection quantity |
| Max | = | maximum value |
| Min | = | minimum value |
| $o$ | = | ambient quantity |
| Ref | = | reference quantity |
| Refresh | = | propellant refresh/refill quantity |
| $t$ | = | total quantity |

*Superscript*

| | | |
|---|---|---|
| $*$ | = | sonic conditions |

## I. Introduction

ROTATING detonation engines (RDEs) have been experimentally shown to provide a viable device in which to implement a pressure gain combustion thermodynamic cycle. Although there are still a number of questions that need to be examined, including many surrounding experimental implementation and loss reduction, the current work will focus on developing a reduced-order thermodynamic modeling procedure for describing the behavior of these engines. The modeling approach selected follows closely the traditional one-dimensional thermodynamic analyses of other airbreathing propulsion systems, such as approaches outlined by Mattingly [1] and the numerical propulsion system simulation (or NPSS) code [2,3]. The model includes the primary thermodynamic cycles that are present in a rotating detonation engine, modeling each in enough detail to adequately capture the device's operation while stopping well short of a full computational fluid dynamic simulation. The agreement of any such model with experimental test results is key to validating this approach and obtaining any utility from the reduced-order procedure. The successful description of the internal thermodynamics of a rotating detonation engine system is vital to optimizing the future application of this pressure gain combustion technology to aerospace propulsion.

## II. Background

The modeling and simulation of rotating detonating engines have been more recently conducted by Parker et al. [3], Schwer and Kailasanath [4–6], Paxson [7], Nordeen et al. [8–12], Davidenko et al. [13], Zhou and Wang [14], and Ibragimov [15]. Schwer and Kailasanath [4,5] developed a numerical procedure for modeling the physics of the flowfield of rotation detonation engines that showed good structural agreement with experimental observations. In addition,

Presented as Paper 2016-1405 at the 54th AIAA Aerospace Sciences Meeting, San Diego, CA, 4–8 January 2016; received 4 March 2016; revision received 13 November 2016; accepted for publication 14 November 2016; published online 16 February 2017. 

*Research Engineer. Associate Fellow AIAA.
†Research Engineer; matt.fotia@gmail.com. Senior Member AIAA.
‡Mechanical Engineer. Associate Fellow AIAA.

they illustrated additional thermodynamic mechanisms with the RDE, including the deflagrative combustion of fuel outside of the detonation wave and the presence of postdetonation shocking of combustion products. These same authors [6] later used this numerical procedure to examine the effects of various engine size parameters that included the nominal diameter, length, and depth of the detonation channel, as well as the area ratio of the propellant injection scheme. Paxson [7] proposed a model that allowed for the reduction of the computational time and resources required to simulate a rotating detonation engine by considering a periodic two-dimensional computational space.

A parametric study of flowfield parameters was conducted by Davidenko et al. [13], in which the injection total pressure and the spatial period of device operation were identified as scaling factors for the geometry and reactive flow pressure, respectively. The average injection mass flux was found to be a factor in driving these two parameters, through the injection pressure ratio applied and the flow dynamics associated with it. Nordeen et al. [9] used the results of detailed numerical simulations of the flowfield inside a rotating detonation engine to examine the various thermodynamic cycles that the working fluid was subjected to in the device. The transfer of energy between the different regions of this same flowfield was later presented [10], whereas divergence, fuel/oxidizer mixing, and area change effects were also examined by Nordeen et al. [8,9].

A similar approach was used by Zhou and Wang [14] to make particle path thermodynamic comparisons between one- and two-dimensional simulations and ideal Zel'dovich–von Neumann–Döring (ZND) model theory. They found qualitative consistency between the different modeling, reporting values for a thermal efficiency of 26.4%, compared to 51.1% for the ideal ZND model. Also, the net mechanical work of 1.1 MJ/kg, or 30% of that expected from the ideal ZND model, was reported. The dynamics of the detonation wave front propagation was expressed analytically in explicit form by Ibragimov [15] for the case of a two-dimensional flowfield with negligible thickness. This analytic approach can more generally be applied to cases where the wave front is known at the initial time and the exact solution is known a priori.

Experimental operation of rotating detonation engines of various configurations have been reported by Shank et al. [16], Naples et al. [17], Fotia et al. [18–20], Russo et al. [21], and Dyer et al. [22]. Shank et al. [16] presented the initial experimental development effort on a nominal 6-in.-diam rotating detonation engine with a focus on mapping the mass flow and equivalence ratio operating space of this new device. Naples et al. [17] examined this device further through the use of a quartz outer body and high-speed chemiluminescence imaging to provide basic data on the various angles present in the flow structure for use in the validation of modeling efforts.

Fotia et al. [18] reported the effects of exhaust flow nozzling on the measured thrust production of a nominal 6-in.-diam rotating detonation engine while examining the comparative effect on performance of both bluff-body and plug-nozzle exhaust schemes. The different regimes of ignition observed in this scale rotating detonation engine were detailed by Fotia et al. [19], where an air ejector configuration was used to provide independent backpressure to the detonation channel. Fotia et al. [20] examined the performance scaling effects as they pertained to the fuel and pressure utilization that occurred with geometric changes to detonation channel width, as well as a comparison of rotating detonation engine performance when operated on hydrogen and gaseous hydrocarbon fuels. Dyer et al. [22] tested a larger-diameter device with a 20 in. detonation channel diameter and found that, for rotating detonation devices, there was a critical interaction between the fuel/air mixing and detonation propagation.

The thermodynamic cycle present in pulsed detonation engine devices has previously been investigated by Heiser and Pratt [23], who proposed a closed thermodynamics cycle analysis of pulsed detonation engines that was independent of time and clarified the fundamental processes at play, whereas Paxson and Kaemming [24] showed the importance of the character of the unsteady pulsed flowfield on the correct calculation of engine performance in the context of pressure gain combustion devices.

## III. Thermodynamic Paths

The computational fluid dynamic solutions of the RDE operation by Schwer and Kailasanath [4–6] provided valuable insight into the major thermodynamic processes within the RDE; see Fig. 1. In this figure, the contours of fluid temperature are shown in the wave frame of reference unwrapped from the RDE cylindrical chamber to a two-dimensional plot. The white lines depict streamline traces of individual fluid particles.

Upon examination, it can be seen that fluid particles 1 to 4 are all processed by the detonation wave in the center of the plot. Of these streamlines, only paths 3 and 4 exit the chamber at the top of the plot without encountering an additional major thermodynamic mechanism. Streamlines 1 and 2 pass through the secondary shock, which is spawned from the detonation wave. Thus, these fluid particles experienced an additional loss associated with the secondary shock.

In the region between streamline 4 and 5, there exist fluid particles that combust subsonically (i.e., deflagrate) when the fresh charge of fuel and air meets the hot products of the detonation. This deflagrated flow is then processed by the strong shock spawned by the detonation wave. Behind the shock, the deflagrated flow begins to mix with the detonated flow, as illustrated by streamline 5. This entire process was explained in more detail by Nordeen et al. [10].

For the current study, the complex flow of the RDE will be summarized using four major thermodynamic processes based upon the major entropy generation mechanisms present in the RDE. The four processes are 1) detonated flow, 2) detonated flow plus secondary shock, 3) deflagrated flow, and 4) a mixed flow comprising both detonated and deflagrated flows. A sample temperature and entropy plot of the major RDE thermodynamic processes assuming an air standard analysis is presented in Fig. 2. Table 1 provides a thermodynamics station numbering reference that will be used to describe the model proposed in this paper.

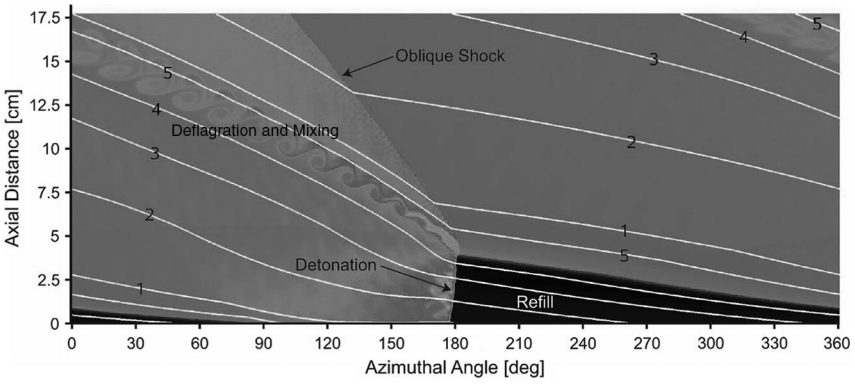


**Fig. 1 Identification of primary thermodynamic flowpaths in a simulated rotating detonation flowfield. Contours of static temperature are shown. Image adapted from the work of Schwer and Kailasanath [5].**

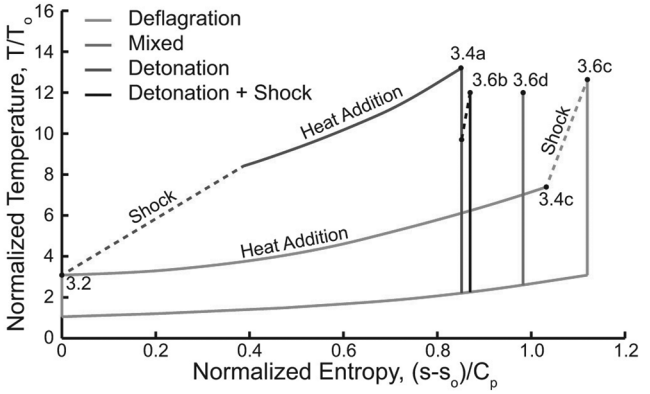


**Fig. 2 Temperature-entropy diagram showing the primary thermodynamic flowpaths in a rotating detonation engine.**



In Fig. 2, the basic detonation process is shown with an assumed normal shock followed by heat addition (i.e., combustion) as fundamentally described by the ZND detonation model. This process results in the least entropy increase due to heat addition within the RDE as a result of the high combustion pressure. After the detonation, this flow turns and accelerates toward the combustor exit. The total temperature of this detonated flow is

$$T_{t3.4a} = T_{3.2}\left(\frac{T_2}{T_1}\right)_{\text{Det}} + \frac{1}{2C_p}\left(a_{3.4a}^2 - V_{\text{Det}}^2 + V_X^2\right) \tag{1}$$

where subscript Det has been used to denote properties of the detonation wave, and $V_X$ represents any gas velocity in the RDE axial direction that may have been present before combustion in the detonation. The total pressure of the flow is found using the second law of thermodynamics and the fact that the change in entropy of the flow is

$$\Delta s_{3.4a} = \Delta s_{3.2} + \Delta s_{\text{Det}} \tag{2}$$

through the detonation wave.

A portion of the flow that is detonated passes through the secondary shock spawned by the detonation wave. This secondary shock results from the internal flows attempting to match flow angles. This is a weak oblique shock, although the turning angle $\theta$ can be significant. The static temperature, pressure, and entropy change across such a shock wave can be written as follows [25]:

$$\frac{T_{3.6b}}{T_{3.4a}} = \frac{\left[2\gamma M_{3.4a}^2\sin^2(\theta) - (\gamma-1)\right]\left[(\gamma-1)M_{3.4a}^2\sin^2(\theta) + 2\right]}{(\gamma+1)^2 M_{3.4a}^2\sin^2(\theta)} \tag{3}$$

$$\frac{P_{3.6b}}{P_{3.4a}} = \frac{2\gamma M_{3.4a}^2\sin^2(\theta) - (\gamma-1)}{\gamma+1} \tag{4}$$

and

**Table 1 Thermodynamic station numbering**

| Station | Detonated | Detonated + shock | Deflagrated | Mixed |
|---|---|---|---|---|
| Injection (air and fuel separate) | 2 | 2 | 2 | — — |
| Precombustion | 3.2 | 3.2 | 3.2 | — — |
| Postcombustion | 3.4*a* | 3.4*b* = 3.4*a* | 3.4*c* | — — |
| Postshock | N/A[a] | 3.6*b* | 3.6*c* | 3.6*d* |
| Nozzle throat | 8 | 8 | 8 | 8 |

[a]Not applicable.

$$\frac{\Delta s_{3.6b}}{C_p} = \ell_n\left(\frac{T_{3.6b}}{T_{\text{Ref}}}\right) - \frac{\gamma-1}{\gamma}\ell_n\left(\frac{P_{3.6b}}{P_{\text{Ref}}}\right) \tag{5}$$

with $M_{3.4s} = V_{\text{Det}}/a_{3.4s}$. These are, of course, the well-known oblique shock formulas with the rotating reference frame of the oblique shock wave taken into consideration. Nonetheless, the entropy generation and total pressure loss created by this shock are relatively small when compared with the detonation shock and the heat addition.

The impinging of the fresh charge of combustion reactants with the hot detonation products results in a portion of the RDE flow being deflagrated. This deflagration is handled in this study as a constant pressure combustion. The current study assumes that all of the deflagrated flow is processed by a strong shock (here assumed normal) immediately above the detonation shock. The total temperature rise across the deflagration is then expressed as

$$T_{t3.6c} = T_{3.4c}\left(\frac{\left[2\gamma M_{3.4c}^2 - (\gamma-1)\right]\left[(\gamma-1)M_{3.4c}^2 + 2\right]}{(\gamma+1)^2 M_{3.4c}^2}\right) + \frac{1}{2C_p}\left(V_{3.6c}^2 - V_{\text{Det}}^2 + V_X^2\right) \tag{6}$$

where $M_{3.4c} = V_{\text{Det}}/a_{3.4c}$, and the velocity of the gas postshock $V_{3.6c}$ is

$$V_{\text{Det}}^2 = a_{3.6c}^2 M_{3.6c}^2 = \frac{(\gamma-1)M_{3.4c}^2 + 2}{2\gamma M_{3.4c}^2 - (\gamma-1)} \tag{7}$$

The resulting total pressure is found similarly to the detonated flow, using the rise in entropy and total pressure across the deflagration/shock process. The result of the constant pressure deflagration and the normal shock is much higher entropy generation when compared with either the detonation flow or the shocked detonation flow.

For the current study, all of the deflagrated flow is assumed to mix with portions of the two detonated flow streams. This done to describe the process that the deflagrated flow undergoes postshock. All of the deflagrated flow will be mixed with some proportion of the two detonated flow streams. The proportions between these streams can be adjusted in the model. In Fig. 2, the mixed flow is shown with entropy mass-averaged properties between the three mixed flows:

$$h_{t3.6d} = Y_c h_{t3.6c} + (1-Y_c)\left[(1-Y_b)h_{t3.6a} + Y_b h_{t3.6b}\right] \tag{8}$$

$$\Delta s_{3.6d} = Y_c \Delta s_{3.6c} + (1-Y_c)\left[(1-Y_b)\Delta s_{3.6a} + Y_b \Delta s_{3.6b}\right] \tag{9}$$

The mass fraction of the mixed flow from the deflagrating stream is denoted by $Y_c$, whereas the portion of the detonated stream that is subjected to the oblique shock wave is $Y_b$ and where $Y_b + Y_c = 1$. Although all of the deflagrated flow is assumed mixed, only a portion of the detonated flows are assumed involved in the mixing. The amount of detonated flows that is mixed is an input parameter to the analysis.

For all of these thermodynamic paths, it is important to remember that the flows are unsteady. Therefore, the peak temperature displayed in Fig. 2 exists only momentarily and is not indicative of the average energy available from the flows. A more detailed description of the proper analysis of pressure gain combustion unsteady flows was presented by Paxson and Kaemming [24].

Finally, the current study turns and accelerates the three exiting flows (i.e., detonation, detonation plus shock, and mixed flows) to the combustor exit. Note that the nozzle throat (station 8) has not been included in Fig. 2, as it would be misleading to associate this station with a single T-s state. This is due to the unsteadiness of the flow, and the distorted velocity profile, out of the nozzle that will be discussed in a later section.

## IV. Propellant Inlet and Exhaust Flow Modeling

To create a usable RDE thermodynamic performance code, a representative model of the propellant injection and of the burned gas exhaust flows must be developed. The function of the inlet flow model is to provide the properties of the incoming propellants as well as the inlet flow rates and the amount of flow that is deflagrated. The function of the exit model is to provide the properties as well as the mass flow rates of that exiting flow. These exit properties can then be used by downstream components, be they turbines or nozzles, to compute performance.

The propellant inlet flow model computes the inlet flow rate based upon the pressure ratio across the inlet by using user-provided propellant inlet performance properties. The pressure ratio across the inlet is computed from the predetonation chamber static pressure and an empirical representation of the decay rate of the detonation pressure, derived from computational fluid dynamics (CFD) results. The empirical pressure decay rate is represented by the following:

$$\tau_{\text{drop}} = 0.00005/\tau_{\text{factor}}$$
$$k = -\ell_n(1-b)/\tau_{\text{drop}}$$
$$P_{3.4}(t)/P_{3.2} = \{1 + [(P_2/P_1)_{\text{Det}} - 1]\exp(-kt)\} \tag{10}$$

where $\tau_{\text{factor}}$ is the decay timing correction factor (typically 1), and $b$ is the pressure drop of 80%.

These empirical factors are controlled by inputs and can be modified if more specific factors are available.

Imposing this time-dependent chamber pressure model onto the user-input inlet performance properties results in a time-dependent inlet mass flow rate. This takes the form of the usual mass flux equation:

$$\frac{\dot{w}(t)}{dA_{\text{Inj}}} = C_w \frac{P_{t2}\sqrt{\gamma}}{\sqrt{RT_{t2}}} M_{\text{Inj}}(t)\left(1 + \frac{\gamma-1}{2}M_{\text{Inj}}^2(t)\right)^{-(\gamma+1)/2(\gamma-1)} \tag{11}$$

but with the time-dependent injection Mach number $M_{\text{Inj}}$ defined by the ratio of propellant manifold total pressure to combustion chamber static pressure

$$M_{\text{Inj}}^2(t) = \frac{2}{\gamma-1}\left[\left(\frac{P_{t2}}{P_{3.4}(t)}\right)^{(\gamma-1)/\gamma} - 1\right] \tag{12}$$

and $C_w$ being the mass flow discharge coefficient. Once the critical pressure ratio is achieved across the injector, the injection Mach number is limited to unity because Eq. (12) will otherwise return supersonic values, which may lead to unphysical results. The total injected mass flow is the summation of the time-dependent mass flow rate over the area of the injector, taking into account the fact that backflowing products must be reintroduced first back into the combustion chamber before fresh reactants can begin to flow.

Knowing the static pressure and the total temperature of the inlet flow, an axial velocity for the flow can be computed, which is represented by $V_{\text{Refresh}}$ in Fig. 3. The portion of the fresh propellants consumed by the deflagration can be computed as a function of time using the flame speed $V_{\text{Flame}}$ at standard conditions, which is then corrected by the code for chamber conditions. By integrating the inlet flow and the flow consumed by the deflagration during a detonation cycle, the procedure computes the amount of fresh flow available for detonation and the amount consumed by the deflagration.

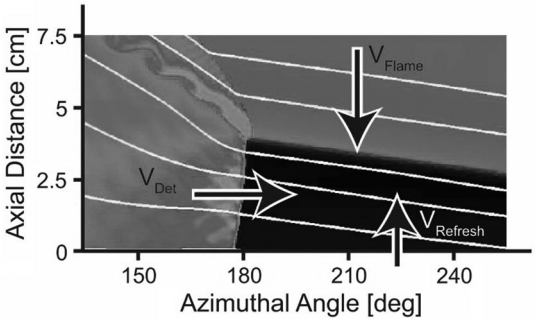


**Fig. 3 Inlet model computing the inlet flow rates and flame speed to determine the ratio of deflagrated and detonated flows. Image adapted from the work of Schwer and Kailasanath [5].**

A comparison of this simplified propellant inlet model was made with higher-order analyses to validate the model. By applying this dynamic inlet flow model to the precombustion conditions quoted by Schwer and Kailasanath [4], a comparison was made, shown in Fig. 4. The simplified propellant inlet model compares well with the higher-order analysis. The higher-order analysis exhibits some subtle effects of weak shock waves within the chamber, which the simplified model ignores. Nonetheless, the maximum propellant flow rates and the total propellant flow rates agree quite well.

The exit flow model currently assumes that all exiting flows are choked at the combustor exit. This assumption has been shown to be sufficient over a wide range of RDE operating conditions. However, because the three flow streams have drastically different flow properties, the flow through the exit is very distorted. Exit flow distortion is defined here as follows:

$$\delta = \frac{V_{8\text{Max}} - V_{8\text{Min}}}{V_{8\text{Avg}}} = \frac{V_{8\text{Max}} - V_{8\text{Min}}}{a_8} \tag{13}$$

where $V_{8\text{Max}}$, $V_{8\text{Min}}$, and $V_{8\text{Avg}}$ are the maximum, minimum, and average axial velocities at the exhaust plane of the RDE. An example of

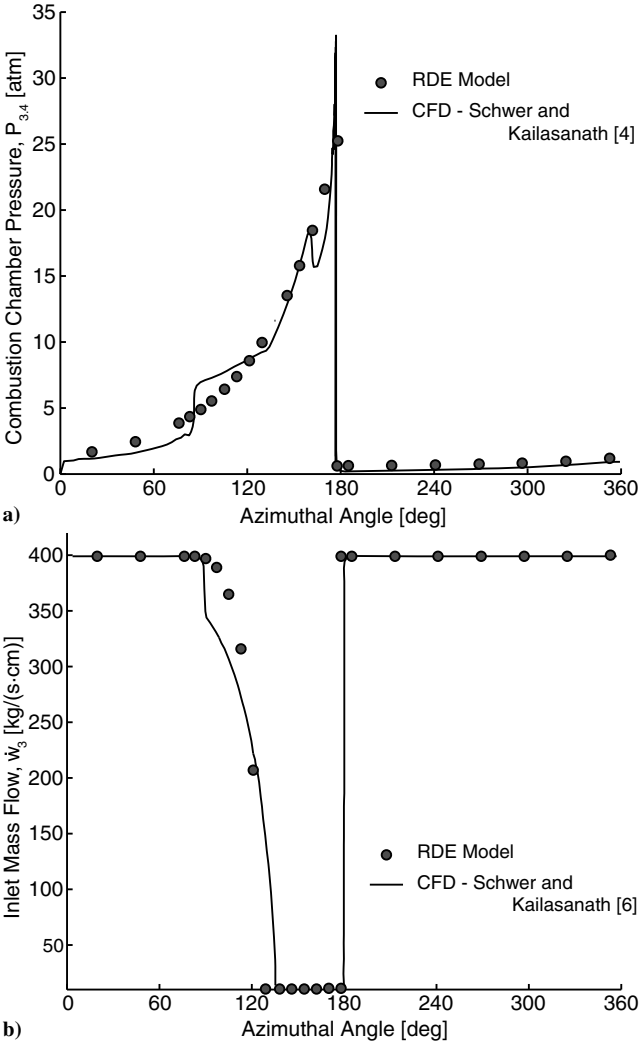


**Fig. 4 Injection model behavior shown in terms of a) detonation chamber static pressure and b) propellant mass flow rate as functions of azimuthal location, and compared to the CFD simulations of Schwer and Kailasanath [4,6].**

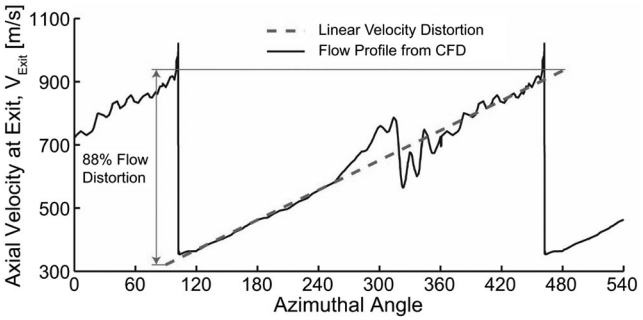


**Fig. 5 Exit flow model behavior shown in terms of axial flow velocity as a function of azimuthal location. Adapted from the work of Schwer and Kailasanath [4].**

the magnitude of exit flow distortion is represented in Fig. 5. The assumption of a choked exit flow requires that $V_{8\mathrm{Avg}}$ be equal to the speed of sound $a_8$, which may not be the case for low $P_{t2}/P_o$. The linear variation of Mach number $M(x)$ in the exit flow can now be written in terms of this distortion

$$M(x) = \delta x + (1 - \delta/2) \tag{14}$$

with $x$ being the normalized circumferential distance along a single wave cycle.

Traditional correlations used for compound flow nozzles cannot be used for RDE analysis because the RDE flow streams are typically mixed subsonic and supersonic flows that inherently violate the compound nozzle assumption of balanced static pressures [26]. To account for the distortion at the RDE exit, correction factors were computed by assuming a distorted isentropic flow relative to a sonic uniform isentropic flow. If the total temperature and pressure of the exit flow are considered constant, the mass flow correction factor for a distorted exit flowfield can be written as

$$\frac{\dot{w}}{\dot{w}*} = \frac{\int_0^1 M(x)/((1 + ((\gamma-1)/2)M(x)^2)^{(\gamma+1)/2(\gamma-1)})\,\mathrm{d}x}{((\gamma+1)/2)^{-(\gamma+1)/2(\gamma-1)}} \tag{15}$$

with the momentum correction factor being

$$\frac{\dot{w}V}{\dot{w}V*} = \frac{\int_0^1 M(x)^2/((1 + ((\gamma-1)/2)M(x)^2)^{\gamma/(\gamma-1)})\,\mathrm{d}x}{((\gamma+1)/2)^{-\gamma/(\gamma-1)}} \tag{16}$$

The resulting correction factors for exit mass flow and exit momentum (Fig. 6) are applied to the computed exit mass flows and momentum. This will allow the use of the mixed thermodynamics flow stream (station 3.6*d*) stagnation properties to be used as an input to the nozzle correction factor model and the model to be iteratively closed as described in the following section.

The exit choke assumption has been shown to be representative over a wide range of RDE operating points. For example, Fig. 7 provides the computed RDE exit mass flow function from the U.S. Air Force Research Laboratory (AFRL) testing. The results show a nearly constant exit throat mass flow function, which is typically attributable to a choked exit. Nonetheless, some recent experiments at very low feed pressures relative to exhaust pressure have shown that the exit flows do not always exhibit these choked characteristics. Therefore, work is ongoing to determine updates to the current exit flow model to properly model RDE operation with low feed pressures.

The construct of any reduced-order thermodynamic analysis, by its very nature, does not directly compute the effects of component efficiencies, axial flow distortion, or any nonaxial flow effects. These performance effects are handled with input efficiency and correction terms. The efficiency factors in the subject analysis include burner combustion efficiency and nozzle stream thrust efficiency. The correction factors include the 1) percentage of detonated flow processed by the secondary shock, 2) percentage of the deflagrated flow that is mixed with detonated flow, 3) amount of nonaxial momentum in the detonated flow, 4) amount of nonaxial momentum in the deflagrated flow, and 5) axial velocity distortion in the exit flow.

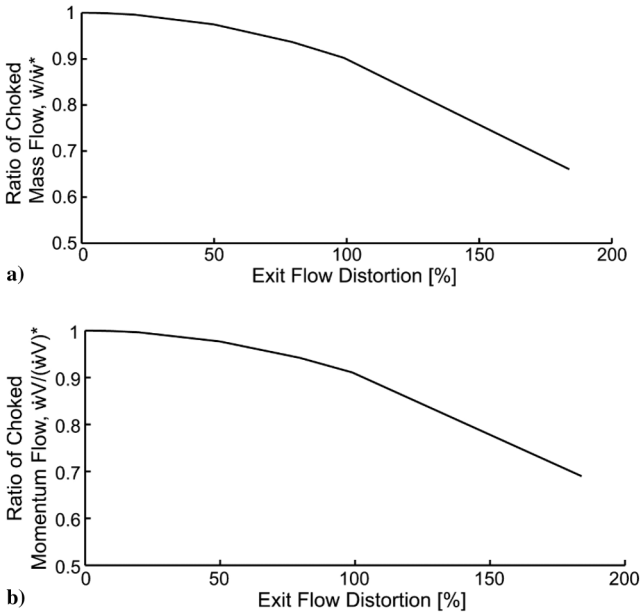


**Fig. 6 Exit flow correction factors for linear velocity distortion with $\gamma = 1.4$.**

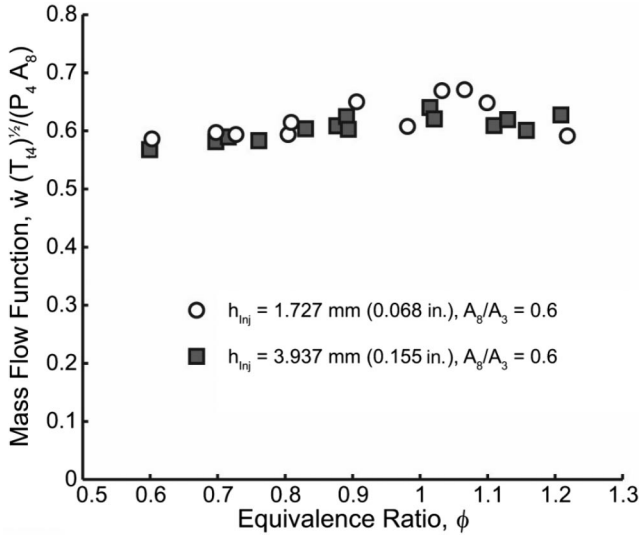


**Fig. 7 Experimental exhaust mass flow function $\dot{w}(T_{t4})^{1/2}/P_4 A_8$, shown as a function of overall equivalence ratio $\phi$ for a nominal 152-mm (6-in.) diameter RDE with a 7.62 mm (0.3 in.) channel width.**

The correction factors are all input as functions of the total combustion chamber height relative to the height of the detonation. The correction factors currently used are derived from two-dimensional flow solutions provided by Dr. Dan E. Paxson of NASA John H. Glenn Research Center.[§]

## V. Inlet and Exit Flow Balancing

With all of the major elements defined, an executive wrapper must be implemented to force conservation of mass; see Fig. 8. The major controlling parameter is the assumed precombustion chamber static pressure $P_{3.2}$. To initiate the process, a precombustion static pressure is assumed that, in turn, is used by the inlet flow model to compute the amount of detonated and deflagrated flows. The thermodynamic model then computes the resultant properties for the multiple streams. The exit flow model then computes the exit flow conditions,

[§]Personal Communication, Oct.–Dec. 2015.

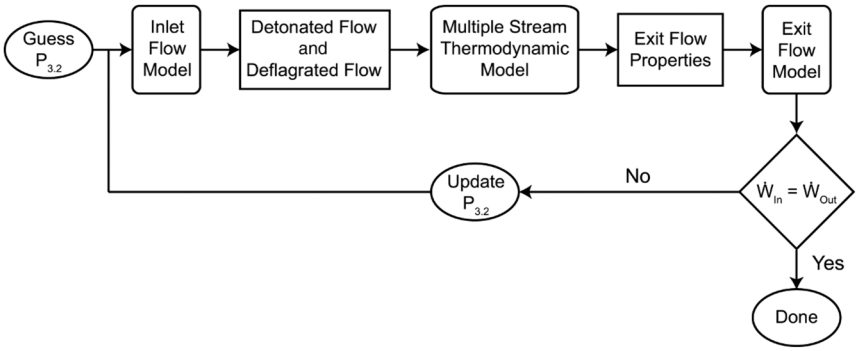


**Fig. 8 Process diagram showing rotating detonation engine model solution procedure.**

including the exit mass flow. The computed exit mass flow is compared to the computed inlet mass flow. If the mass flows do not agree, the precombustion static pressure is updated and the process repeated until the inflow and outflow agree.

## VI. Model Validation

Careful validation of the current model has been done with comparisons to both high-fidelity CFD simulation results and experimentally measured RDE performance. Figure 9 shows that the model-generated solutions provide good agreement with the experimental test data. In this case, the data are for operation of a 152.4 mm (6 in.) nominal diameter RDE with a 7.62 mm (0.3 in.) width detonation channel, operating at various equivalence ratios of gaseous hydrogen and air. It should be noted that the only inputs provided to the model are the propellant feed pressures and the basic geometric parameters of the RDE tested. The model captures the major loss mechanisms present in the RDE adequately enough that both the computed specific thrusts $F_{sp}$ (shown in Fig. 9a) and the specific impulses $I_{sp}$ (shown in Fig. 9b) agree within experimental error across the range of tested equivalence ratios. The specific thrust is defined here as $F_{sp} = F_g/\dot{m}_{Air}$ and the specific impulse is defined as $I_{sp} = F_g/\dot{m}_{Fuel} g_o$, using the usual airbreathing definition.

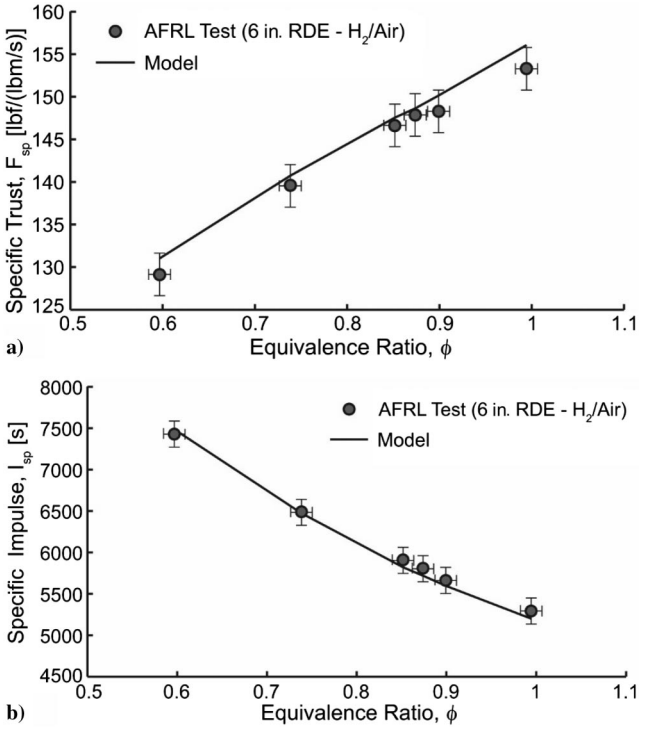


**Fig. 9 Model validation with measured experimental rotating detonation engine performance: a) specific thrust $F_{sp}$, and b) specific impulse $I_{sp}$ shown as a function of the global combustor equivalence ratio $\phi$.**

CFD allows for a closer examination of the computed model solutions, in which quantities difficult to measure experimentally can be compared. The key parameter that is adjusted to provide closure of the mass flow rates through the inlet and exhaust models is the precombustion static pressure $P_{3.2}$. Schwer and Kailasanath [6] found that there was a direct relationship between the ratio of the propellant injection area to that of the detonation channel $A_{Inj}/A_3$ and the resulting precombustion static pressure in the detonation channel once the mass flows into and out of the device were balanced. The present model reproduces this behavior as shown in Fig. 10a, along with the values published by Schwer and Kailasanath [6]. A set of modeled conditions where lateral detonation area relief is allowed are also provided in the figure, where a very minor impact on precombustion static pressures can be seen. This difference becomes imperceptible as the injection area ratio is increased. For completeness, the static temperature and pressure ratios across the detonation with lateral area relief are

$$\frac{T_2}{T_1} = \frac{C_{p1}(1 + ((\gamma_1 - 1)/2)M_{Det}^2 + \tilde{q})}{C_{p2}((\gamma_2 + 1)/2)} \tag{17}$$

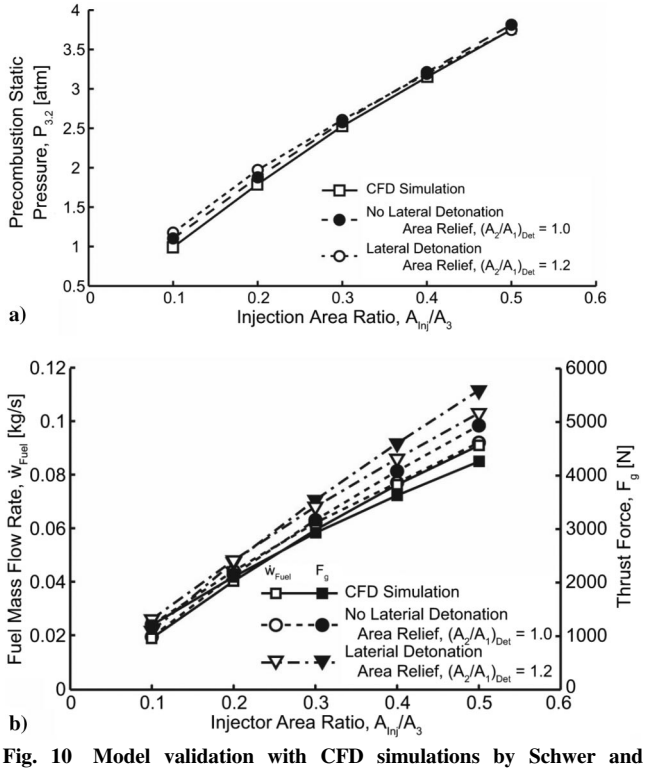


**Fig. 10 Model validation with CFD simulations by Schwer and Kailasanath [6] of a rotating detonation engine showing a) static pressure before detonation $P_{3.2}$, and b) fuel mass flow rate $\dot{m}_{Fuel}$ and thrust $F_g$ as a function of the propellant injector area ratio $A_{Inj}/A_3$.**

and

$$\frac{P_2}{P_1} = \frac{1 + \gamma_1 M_{\text{Det}}^2}{1 + (A_2/A_1)\gamma_2} \tag{18}$$

where the pre- and postdetonation states have been denoted by subscripts 1 and 2, respectively. The Mach number of the detonation is found through the iterative solution to the balance of energy, which takes the form

$$\frac{1 + \gamma_1 M_{\text{Det}}^2}{M_{\text{Det}}}\left[\frac{(\gamma_2 + 1)/2}{1 + ((\gamma_1 - 1)/2)M_{\text{Det}}^2 + \tilde{q}}\right]^{1/2} = \left(\frac{A_1}{A_2} + \gamma_2\right)\frac{\gamma_1}{\gamma_2}\left[\frac{\gamma_2 - 1}{\gamma_1 - 1}\right]^{1/2} \tag{19}$$

with $\tilde{q}$ being the energy deposited by the consumed fuel normalized by $C_{p1}T_1$.

A similar comparison is made between the resulting fuel mass flow rate $\dot{w}_{\text{Fuel}}$ and gross thrust $F_g$. In this instance, as the propellant injection area is increased, some slight divergence can be seen between the model values and those from the CFD simulations. The largest difference is on the order of less than 5% of either parameter. Again, the model solutions with no lateral detonation area relief provide closer agreement with the high-fidelity CFD results.

## VII. Performance Parameters

### A. Detonating Versus Deflagrating Combustion

One of the primary loss mechanisms in a RDE is premature deflagration of propellants before being consumed through detonation in the propagating wave. A result of describing the inlet flow to the RDE as it has been in the model is that the proportion of the propellant flow deflagrated is a dependent variable and is subject to the mechanics of the rest of the model.

The influence of deflagration on overall performance and the inlet/exhaust model mass balancing is presented in Fig. 11, where the ideal specific impulse $I_{\text{sp}}$ resulting from two different combustor pressure assumptions is given. A constant chamber pressure is assumed for the dashed line; whereas, for the solid line, the chamber pressure is calculated to allow for the balancing of the injected and exhausted mass flows.

As the mass fraction of the flow that is deflagrated increases, the specific impulse under constant combustion chamber pressure conditions decreases linearly. This is a direct result of the increased entropy generated by deflagration when compared with detonation. When conservation of mass in and out of the combustor is considered, the performance is relatively constant at low percentages of deflagration. This results from the lower mass flux of the deflagrated flow, which in turn increases the chamber pressure that leads to improved performance. Eventually, the entropy increase of the deflagration becomes the dominant influence, resulting in the expected rolloff at high ratios of deflagrated flow.

The impact of the conservation of mass on the precombustion static pressure $P_{3,2}$ is given in Fig. 12 as a function of the mass fraction of the flow deflagrated. As less of the reactants are detonated, and more deflagrated, the precombustion pressure required to balance the mass injected and exhausted from the chamber increases. It should be noted that, as the precombustion pressure increases, so will the propellant feed pressures required to maintain a constant mass flow rate through the RDE. The total mass flow rate has not been held constant along the curves shown in Fig. 11 or Fig. 12, but only geometry and propellant feed pressures.

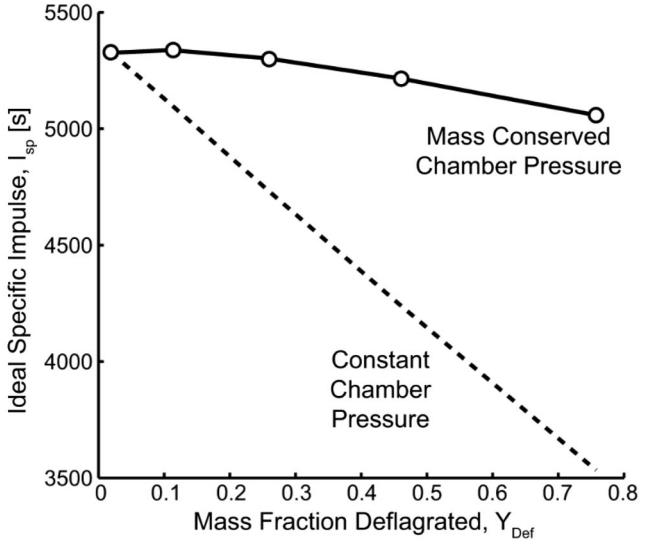


**Fig. 11 Comparison of ideal specific impulse $I_{\text{sp}}$ calculated from injector/exit flow balancing and ideal constant chamber pressure model.**

### B. Precombustion Pressure

Figure 13 shows how the variation of precombustion static pressure impacts RDE performance and is a function of both the injection geometry and the propellant pressures provided. Considering a single air feed pressure, changes in the propellant injection area ratio allow for an increase in precombustion static pressure by a factor of two to three, dependent on feed conditions. This results in a factor of five to eight increase in specific impulse.

An alternative way to view this relationship is that, for a set injection geometry, an increase in the air feed pressure will also result

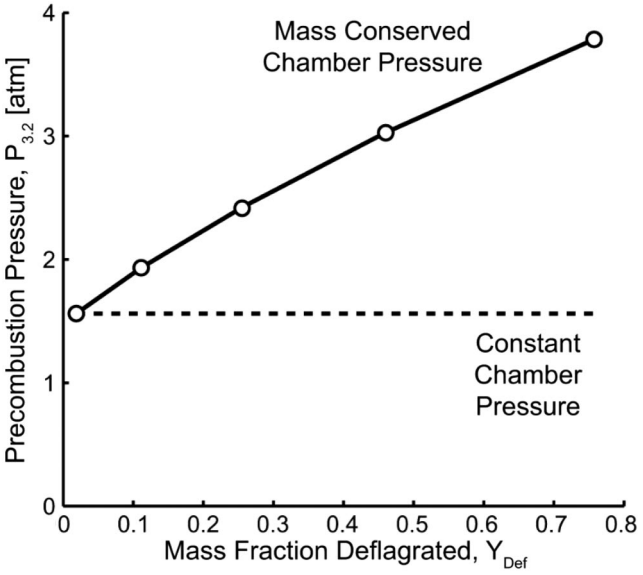


**Fig. 12 Comparison of precombustion pressure $P_{3,2}$ calculated from injector/exit flow balancing and ideal constant chamber pressure model.**

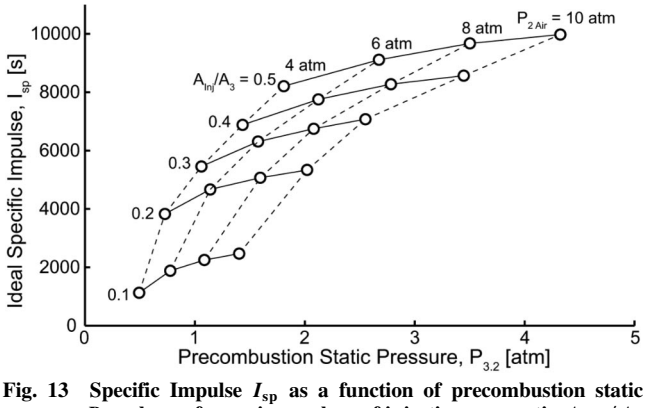


**Fig. 13 Specific Impulse $I_{\text{sp}}$ as a function of precombustion static pressure $P_{3,2}$, shown for various values of injection area ratio $A_{\text{Inj}}/A_3$ and air injection pressure $P_{2\text{Air}}$.**

in an increase in the predetonation static pressure. However, unlike an injection area ratio increase where static pressure is increased through the requirement to balance injected and exhausted mass, an increase in air feed pressure simply increases the total pressure of the gas that is then expanded into the combustion chamber.

### C. Lateral Detonation Area Relief

The presence of lateral detonation area relief must be looked at from two different perspectives. The first is that nonconfinement of the detonating fill gases has the potential to drive losses in performance. Second, this area change through the detonation wave will create a deficit in the observed propagation velocity of the detonation. Lateral detonation area relief is defined here as the difference in the area through which the reactant enters the detonation wave $A_{1\mathrm{Det}}$ relative to the area through which the detonated exhaust products exit the wave $A_{2\mathrm{Det}}$.

To evaluate the first concern, model solutions for cases with no lateral detonation area relief $[(A_2/A_1)_{\mathrm{Det}} = 1.0]$, 20% relief $[(A_2/A_1)_{\mathrm{Det}} = 1.2]$, and 40% relief $[(A_2/A_1)_{\mathrm{Det}} = 1.4]$ are given as a function of equivalence ratio in Fig. 14a. Across all three area ratios considered, there is a very minor variation in the calculated specific impulse. As shown in the lower panel of the figure (Fig. 14b), these differences are less than 2.5% relative to the case with no lateral area relief. There does exist a crossover point at an equivalence ratio of approximately 0.75 where any lateral relief may begin to actually increase the performance of the RDE through reduction in shock velocities and their associated stagnation pressure losses.

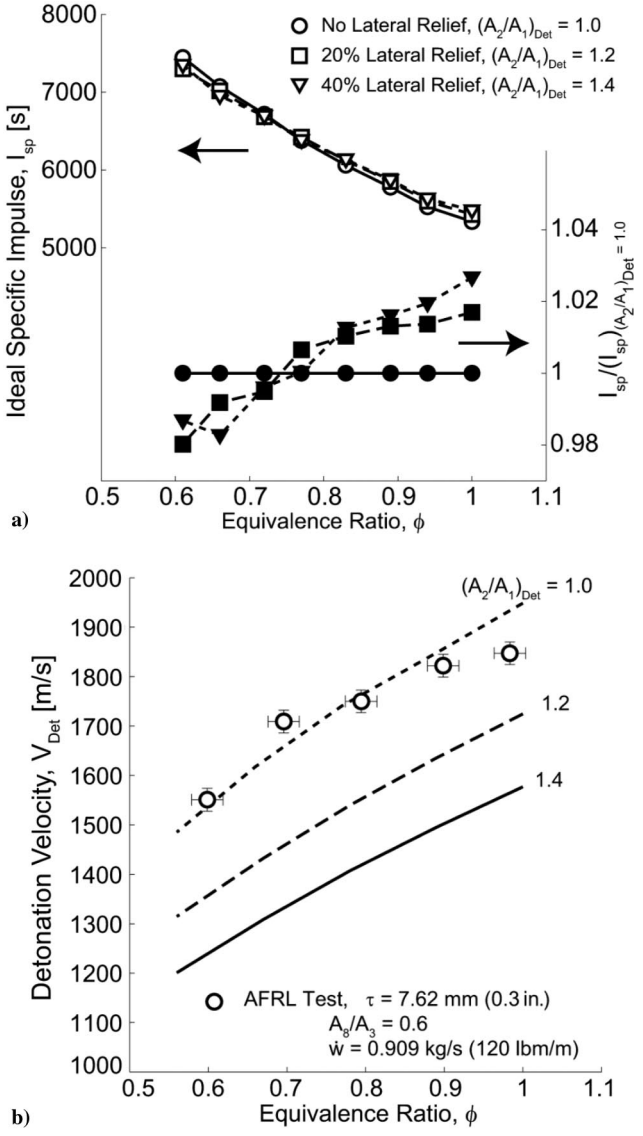


**Fig. 14 Impact of lateral area relief through detonation shown in terms of a) specific thrust $F_{sp}$, and b) detonation velocity $V_{Det}$ as a function of equivalence ratio $\phi$.**

The computed detonation velocities under the same levels of lateral detonation area relief are compared to experimental values, the operating conditions of which were used to produce the model results as seen in Fig. 14b. The experimental values show variation along the no lateral relief curve, $(A_2/A_1)_{\mathrm{Det}} = 1.0$, in which a maximum of 10% area relief might be required to explain the lower than Chapman–Jouget velocity results from the experiment.

Experimental RDE observations of detonation velocities can result in even lower values than those reported here. An explanation of these observations is simply a larger apparent amount of lateral area relief through the detonation that results in a very small variation in RDE performance.

The results of this study show that lateral relief in an RDE combustor produces detonation velocities less than the classical Chapman–Jouget velocities. These lower detonation velocities, however, have only a minor influence on the performance developed by a RDE.

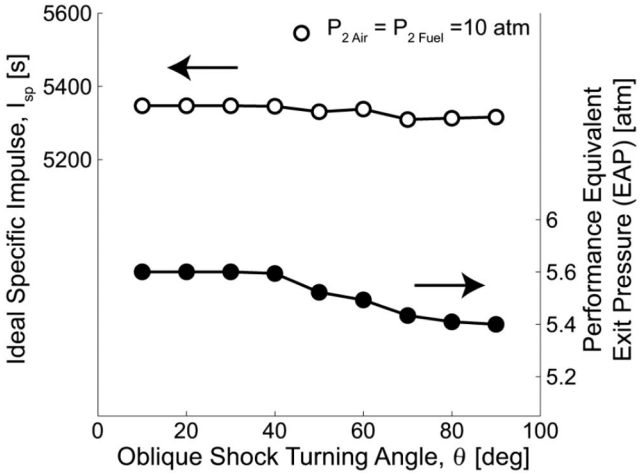


**Fig. 15 Impact of variation in oblique shock turning angle $\theta$ on ideal specific impulse $I_{sp}$ and performance equivalent exit pressure (EAP).**

### D. Secondary Shock Strength

The one RDE flow feature that has not been directly examined thus far is the oblique shock wave that is produced through the interaction of the detonated gases with the products of the previous detonation cycle. The model that has been presented treats this interaction as a constant with a set turning angle, even though variations in gas temperatures and compositions will alter the relationship.

However, as can be seen in Fig. 15, where the specific impulse is given as a function of oblique shock turning angle $\theta$ for set feed conditions, the attained specific impulse is relatively insensitive to even a normal shock ($\theta = 90$ deg), which is not strictly possible. The performance equivalent available pressure (EAP) is also provided in the figure. The EAP is defined as the equivalent steady-state chamber total pressure that will provide the same ideal thrust as the actual, unsteady case. Based on thrust, it follows that the EAP exhibits a similar insensitivity to the turning angle as that exhibited in an ideal specific impulse. However, the EAP can also be viewed as providing a gauge of the impact of the destruction of available stagnation pressure across the shock wave. In the lower portion of Fig. 15, the EAP can be seen to only decrease by 0.2 atm, or ~4%, over the full range of angles considered.

## VIII. Conclusions

A reduced-order thermodynamic model of a rotating detonation engine has been developed in which multiple internal thermodynamic pathways have been coupled to component models of the

propellant injection and exhaust processes. This approach built on previous high-fidelity computational simulations of the flowfield internal to an RDE, as well as experimental testing of these novel pressure gain combustion devices.

The solutions created by this modeling effort have been validated through comparison with both the high-fidelity simulations of other authors and experimentally measured performance data of actual operating RDE test sections. These comparisons showed that the model provided good agreement in the key areas of precombustion static pressure and the resulting performance created.

The influence of various loss mechanisms have been examined. The mass fraction of the flow deflagrating before detonation and the fluid mechanical interaction of the propellant injectors with the unsteady detonation chamber flowfield, as varied through injection area, have been found to be major drivers of system performance. This was in contrast to the relative speed of the detonation wave that might be present in the flowfield, or the exact turning angle of the oblique shock wave, which showed minor influences on the overall device behaviors.

The use of such a reduced-order thermodynamic model to better understand the global design space of rotating detonation engines can be critical in resource-constrained environments if other more resource-intensive methods of analysis, such as CFD or experimentation, are to be efficiently used to further the development of this promising pressure gain combustion technology.



## References


[1] Mattingly, J. D., *Elements of Propulsion: Gas Turbines and Rockets*, AIAA Education Series, AIAA, Reston, VA, 2006, Chap. 4, 8.

[2] Lytle, J. K., "The Numerical Propulsion System Simulation: A Multidisciplinary Design System for Aerospace Vehicles," NASA TM-1999-209194, July 1999.

[3] Parker, K. I., Felder, J. L., Lavelle, T. M., Withrow, C. A., Yu, A. Y., and Lehmann, W. V. A., "Integrated Control Modeling for Propulsion Systems Using NPSS," NASA TM-2004-212945, Feb. 2004.

[4] Schwer, D. A., and Kailasanath, K., "Numerical Investigation of the Physics of Rotating-Detonation-Engines," *Proceedings of the Combustion Institute*, Vol. 33, No. 2, 2011, pp. 2195–2202. doi:10.1016/j.proci.2010.07.050

[5] Schwer, D. A., and Kailasanath, K., "Numerical Investigation of Rotating Detonation Engines," *46th Joint Propulsion Conference and Exhibit*, AIAA Paper 2010-6880, 2010. doi:10.2514/6.2010-6880

[6] Schwer, D. A., and Kailasanath, K., "Numerical Study of the Effects of Engine Size on Rotating Detonation Engines," *49th AIAA Aerospace Sciences Meeting*, AIAA Paper 2011-0581, 2011. doi:10.2514/6.2011-581

[7] Paxson, D., "Numerical Analysis of a Rotating Detonation Engine in the Relative Reference Frame," *52nd AIAA Aerospace Sciences Meeting*, AIAA Paper 2014-0284, 2014. doi:10.2514/6.2014-0284

[8] Nordeen, C. A., Schwer, D., Schauer, F., Hoke, J., Barber, T., and Cetegen, B., "Thermodynamics Model of a Rotating Detoantiom Engine," *Combustion, Explosions and Shock Waves*, Vol. 50, No. 5, 2014, pp. 568–577. doi:10.1134/S0010508214050128

[9] Nordeen, C., Schwer, D., Schauer, F., Hoke, J., Cetegen, B., and Barber, T., "Thermodynamic Modeling of a Rotating Detonation Engine," *49th AIAA Aerospace Sciences Meeting*, AIAA Paper 2011-0803, 2011. doi:10.2514/6.2011-803

[10] Nordeen, C., Schwer, D., Schauer, F., Hoke, J., Barber, T., and Cetegen, B., "Energy Transfer in a Rotating Detonation Engine," *47th AIAA/ASME/SAE/ASEE Joint Propulsion Conference*, AIAA Paper 2011-6045, 2011. doi:10.2514/6.2011-6045

[11] Nordeen, C., Schwer, D., Schauer, F., Hoke, J., Barber, T., and Cetegen, B., "Divergence and Mixing in a Rotating Detonation Engine," *51st AIAA Aerospace Sciences Meeting*, AIAA Paper 2013-1175, 2013. doi:10.2514/6.2013-1175

[12] Nordeen, C., Schwer, D., and Corrigan, A., "Area Effects on Rotating Detonation Engine Performance," *50th AIAA/ASME/SAE/ASEE Joint Propulsion Conference*, AIAA Paper 2014-3900, 2014. doi:10.2514/6.2014-3900

[13] Davidenko, D. M., Gokalp, I., and Kudryavtsev, A. N., "Numerical Study of the Continuous Detonation Wave Rocket Engine," *15th International Space Planes and Hypersonic Systems and Technologies Conference*, AIAA Paper 2008-2680, 2008. doi:10.2514/6.2008-2680

[14] Zhou, R., and Wang, J.-P., "Numerical Investigation of Flow Particle Paths and Thermodynamic Performance of Continuously Rotating Detonation Engines," *Combustion and Flame*, Vol. 159, No. 12, 2012, pp. 3632–3645. doi:10.1016/j.combustflame.2012.07.007

[15] Ibragimov, R. N., "Multidimensional Wave Fronts Propagation Along the Beams Associated with Thermodynamic Model of a Rotating Detonation Engine," *Applied Mathematical Modelling*, Vol. 40, No. 4, 2016, pp. 2661–2673. doi:10.1016/j.apm.2015.09.027

[16] Shank, J. C., King, P. I., Karnesky, J., Schauer, F., and Hoke, J. L., "Development and Testing of a Modular Rotating Detonation Engine," *50th AIAA Aerospace Sciences Meeting Including the New Horizons Forum and Aerospace Exposition*, AIAA Paper 2012-0120, 2012. doi:10.2514/6.2012-120

[17] Naples, A., Hoke, J., Karnesky, J., and Schauer, F., "Flowfield Characterization of a Rotating Detonation Engine," *51st AIAA Aerospace Sciences Meeting Including the New Horizons Forum and Aerospace Exposition*, AIAA Paper 2013-0278, 2013. doi:10.2514/6.2013-278

[18] Fotia, M., Schauer, F., Kaemming, T., and Hoke, J., "Experimental Study of the Performance of a Rotating Detonation Engine with Nozzle," *Journal of Propulsion and Power*, Vol. 32, No. 3, 2016, pp. 674–681. doi:10.2514/1.B35913

[19] Fotia, M. L., Schauer, F., and Hoke, J. L., "Experimental Ignition Characteristics of a Rotating Detonation Engine Under Backpressured Conditions," *53rd AIAA Aerospace Sciences Meeting*, AIAA Paper 2015-0632, 2015. doi:10.2514/6.2015-0632

[20] Fotia, M. L., Hoke, J. L., and Schauer, F., "Experimental Performance Scaling of Rotating Detonation Engines Operated on Gaseous Fuels," *Journal of Propulsion and Power* (accepted for publication).

[21] Russo, R., King, P. I., Schauer, F., and Thomas, L. M., "Characterization of Pressure Rise Across a Continuous Detonation Engine," *47th AIAA/ASME/SAE/ASEE Joint Propulsion Conference*, AIAA Paper 2011-6046, 2011. doi:10.2514/6.2011-6046

[22] Dyer, R., Naples, A., Kaemming, T., Hoke, J., and Schauer, F., "Parametric Testing of a Unique Rotating Detonation Engine Design," *50th AIAA Aerospace Sciences Meeting Including the New Horizons Forum and Aerospace Exposition*, AIAA Paper 2012-0121, 2012. doi:10.2514/6.2012-121

[23] Heiser, W. H., and Pratt, D. T., "Thermodynamics Cycle Analysis of Pulsed Detonation Engines," *Journal of Propulsion and Power*, Vol. 18, No. 1, 2002, pp. 68–76. doi:10.2514/2.5899

[24] Paxson, D. E., and Kaemming, T., "Influence of Unsteadiness on the Analysis of Pressure Gain Combustion Devices," *Journal of Propulsion and Power*, Vol. 30, No. 2, 2014, pp. 377–383. doi:10.2514/1.B34913

[25] "Equations, Tables, and Charts for Compressible Flow," NACA, Ames Aeronautical Lab. TR 1135, Moffett Field, CA, 1 Jan. 1953.

[26] Bernstein, A., Heiser, W., and Hevenor, C., "Compound-Compressible Nozzle Flow," *AIAA 2nd Joint Propulsion Specialists Conference*, AIAA Paper 1966-0663, 1966.


V. Raman
*Associate Editor*